RSC Advances

Electrochemical Performances of CoFe2O4 nanoparticles and rGO based asymmetric supercapacitor

Journal:	*RSC Advances*
Manuscript ID	RA-ART-07-2015-014938.R2
Article Type:	Paper
Date Submitted by the Author:	22-Oct-2015
Complete List of Authors:	Ramakrishnan, Kalai; Bharathiar University, Physics Vijaya Sankar, Kalimuthu; Bharathiar University, Physics Meyrick, Danielle; Murdoch University, School of Chemical and Mathematical Sciences
Subject area & keyword:	Energy research < Physical

Journal Name

RSCPublishing

ARTICLE

Cite this: DOI: 10.1039/x0xx00000x
Received 00th November 2013,
Accepted 00th November 2013
DOI: 10.1039/x0xx00000x
www.rsc.org/

Electrochemical performances of $CoFe_2O_4$ nanoparticles and rGO based asymmetric supercapacitor

K. Vijaya Sankar[a], R. Kalai Selvan[a]*, Danielle Meyrick[b]

$CoFe_2O_4$ nanoparticles were prepared using a polyethylene glycol (PEG) assisted solution combustion method. The X-ray diffraction pattern and Fourier Transform Infrared spectra revealed the single phase formation of $CoFe_2O_4$ particles. Transmission electron microscope (TEM) images revealed nanosized particles less than 10 nm in size. The calculated voltammetry specific capacitance of the $CoFe_2O_4$ electrode was 195 Fg^{-1} at 1 mV s^{-1}. The Powers law suggests the capacitive mechanism is dominant over an intercalation mechanism, while the maximum number of charges accommodated in the inner surface of the electrode, is given by the Trasatti plot. The fabricated rGO based hybrid supercapacitor ($CoFe_2O_4$||rGO) provides a good specific capacitance (38 Fg^{-1}) and energy density (12.14 Wh kg^{-1}) at 3 mA with good cycle life, and the serially connected asymmetric supercapacitor device powers the light emitting diode for 10 minutes.

1. Introduction

Both renewable and non-renewable energy sources are currently meeting global energy requirements, but the availability of non-renewable energy sources, particularly fossil fuels, is diminishing rapidly due to increasing use of electrical and electronic equipment and automobiles and, importantly, the increasing human population. In addition, energy production from renewable energy sources is seasonal and dependent upon climatic conditions, creating the need for energy storage devices. The presently available energy storage and conversion devices include batteries, fuel cells, conventional capacitors and supercapacitors. Batteries and fuel cells are primarily used in high energy applications, while conventional capacitors are used for high power applications, as seen in the Ragone plot.[1] Significant research and development effort has focused on developing alternative devices that satisfy both high power and high energy requirements, and supercapacitors fulfil these criteria. These devices have a wide range of potential applications, including hybrid electrical vehicles, 'smart' devices, tablets and so on.

Based on the charge storage mechanism and characteristics of electrode materials, supercapacitors may be categorised as (i) electrical double layer capacitor (EDLC); (ii) pseudocapacitor; and (iii) hybrid supercapacitor. In the EDLC, the charge is stored by the formation of a double layer at the electrode/electrolyte interface *via* electrostatic attraction. Normally, EDLCs deliver high power density and a long cycle life, but provide lower energy density than batteries. On the other hand, pseudocapacitors store charge through surface redox reactions or electron transfer reactions, and deliver higher energy density but inferior cycling stability. In the hybrid supercapacitor, one electrode stores the charge based on the electrical double layer formation, while surface redox reactions store the charge in the other electrode. The advantages of each mechanism are exploited in the hybrid device.

Different metal oxides and conducting polymers have been employed as electrodes for pseudocapacitors.[2] Among the mixed metal oxides, spinel ferrites have unique physical and chemical properties such as chemical stability, a range of oxidation states, hard and soft magnetic properties, and superparamagnetism.[3-5] Various spinel ferrites, including $MnFe_2O_4$, $ZnFe_2O_4$, $CoFe_2O_4$ and $NiFe_2O_4$, have been identified as potential electrodes for supercapacitor applications.[6-8] $CoFe_2O_4$ has diverse properties, including high specific capacitance (372 mAh g^{-1}), excellent chemical stability, and efficient

electrocatalytic behaviour, and has been prepared by hydrothermal, solvothermal, microwave, and auto combustion methods.[9-15a]

To the best of our knowledge, there is no published report of polyethylene glycol (PEG) assisted solution combustion synthesis of $CoFe_2O_4$ porous particles. Here, PEG acts as a surfactant which controls the particle size, thus avoiding the need for subsequent high temperature calcination of the material produced.[15b] Overall, this synthesis method is simple, inexpensive, has a short reaction time, good molecular level mixing, induces an exothermic reaction and creates pores on the particle surface.[15c] Birol et al have reported that the solution combustion is the suitable technique for the industrial or large scale production of samples.[15c] In this study, $CoFe_2O_4$ electrodes are prepared and subjected to structural and electrochemical analysis and thus evaluated for possible pseudocapacitor applications. Using Power's Law and the Trasatti plot, the surface charge storage mechanism is identified and the charge stored in the inner and outer surface of the electrodes calculated. Finally, an asymmetric hybrid supercapacitor is fabricated using rGO as the positive electrode and the electrochemical performance studied. To the best of our knowledge, this is the first report on the surface charge storage mechanism of $CoFe_2O_4$ electrodes in 1M KOH aqueous electrolyte.

2. Experimental methods and materials

For the typical synthesis, stoichiometric quantities of $Co(NO_3)_2.6H_2O$, $Fe(NO_3)_3.9H_2O$, and glycine were dissolved in the desired volume of distilled water. The required quantity of PEG was added to the resulting solution at 15 minute intervals and stirred vigorously. The final solution was placed on a hot plate to facilitate removal of water and allow the formation of metal-fuel complexes. The dry gel obtained was immediately transferred into an electric heater to initiate the combustion reaction. After completing the combustion reaction, the resulting foamy powder was ground well for further studies. The procedure was repeated for the preparation of material utilising different PEG concentrations during the reaction; 8 mL (CC-1), 9 mL (CC-2) and 10 mL (CC-3).

The phase purity, crystallinity, and the functional groups present in the synthesised material were analysed using Bruker D8 Advance XRD with Cu Kα radiation and Bruker Tensor27 FT-IR instruments. The morphological features of the sample were determined using HRTEM (JEOL JEM 2100). The electrical behaviour of the material was studied using a computer controlled impedance analyzer HIOKI 3532 LCR HITESTER in the frequency range 42 Hz to 4 MHz. The powder sample was pressed into a 1 cm diameter pellet at a pressure of 50 kg cm^{-2} under identical conditions for each analysis. A Bio-logic VSP3 electrochemical workstation was used for evaluating the electrochemical properties of the samples.

The active electrode was prepared by mixing $CoFe_2O_4$ (30 mg), carbon black (6 mg), and polyvinlidene difluoride (PVDF) (2 mg) (i.e., mass ratio 80:15:5) with 0.3 mL of N-methyl 2-pyrrolidine (NMP) to produce an homogeneous slurry. Twenty micro litres of the slurry was coated onto a stainless steel (SS) substrate. The prepared electrode was dried at 60˚C overnight in a vacuum oven. The resulting active mass of the coated electrode was 2 mg. The same procedure was followed for the rGO electrode preparation, but 0.4 mL of NMP and electrode mass of 1.5 mg. Electrodes were separated by a polypropylene sheet in the asymmetric supercapacitor. Before electrochemical investigation, the electrodes and separator were immersed in aqueous electrolyte for one hour.

3. Results and Discussion

Structural and morphological analysis

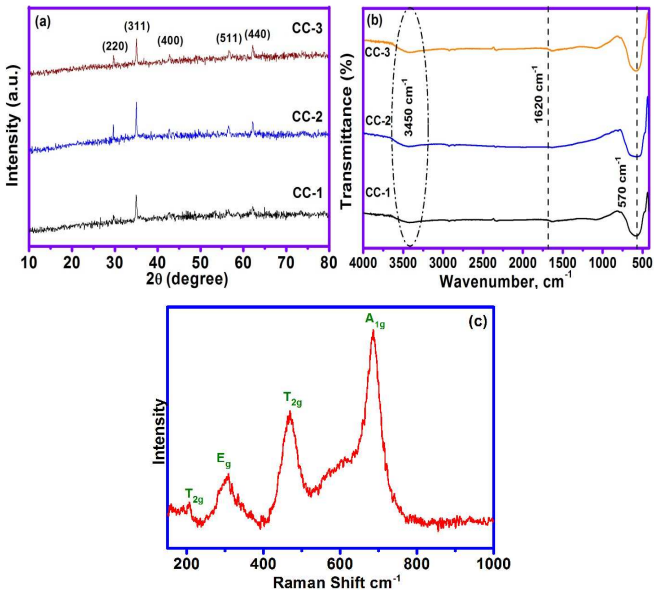

Fig. 1. (a) XRD pattern, (b) FT-IR spectra, and (c) Raman spectrum of $CoFe_2O_4$ nano particles.

The XRD analysis was carried out to identify the phase purity and crystallinity of the samples. Fig. 1 (a) shows the XRD pattern of $CoFe_2O_4$ particles prepared at different PEG concentrations. The observed

sharp and well-defined peaks indicate good crystallinity of the samples. The diffraction peaks at 29.636˚, 35.00˚, 42.68˚, 56.52˚ and 62.12˚ reveal the formation of single phase $CoFe_2O_4$. The calculated lattice constants are 8.4743Å, 8.4751Å and 8.4610 Å for CC-1, CC-2 and CC-3, respectively, which agree well with standard data (JCPDS no.:22-1086), further confirming the formation of single phase $CoFe_2O_4$ with a cubic structure. The grain sizes calculated using the Scherrer equation[16-18] are 33, 47 and 36 nm for CC-1, CC-2 and CC-3 respectively. FT-IR spectra (Fig. 1(b)) reveals M-O (M= Fe, Co) stretching vibration modes at 570 and 700 cm^{-1}, further supporting the formation of $CoFe_2O_4$. However, the expected peak (Co-O) at 700 cm^{-1} is not clearly visible due to the weak absorption and broadening of the Fe-O stretching vibration mode.[19,20a] The observed absorption peaks at 1620 and 3450 cm^{-1} correspond to water, while the absence of peaks corresponding to organic functional groups indicates the complete burning of PEG during the combustion reaction.

Raman spectroscopy is a sensitive and non-destructive technique that reveals information relating to local distortion, cation distribution, strain and magnetic disordering in spinel structured materials. Fig. 1(c) is the Raman spectrum of spinel $CoFe_2O_4$ nanoparticles. According to Group Theory, this material consists of five Raman active modes, including $3T_{2g}$, E_g, A_{1g}.[20b,20c] Two broad and low intensity peaks are observed at 205 cm^{-1} and 308 cm^{-1}, corresponding to the T_{2g} and E_g vibration modes respectively. Strong and intense peaks are noticed at 467 cm^{-1} and 687 cm^{-1} that correspond to the T_{2g} and A_{1g} modes of vibration. Here, the T_{2g} modes relate to the lattice vibration or oxygen motion in the octahedral sites of spinel $CoFe_2O_4$. Similarly, the A_{1g} mode illustrates the vibration arising from tetrahedral sites or oxygen motion around tetrahedral sites of spinel $CoFe_2O_4$. The Raman spectra support the XRD and FT-IR results.

Representative TEM images of CC-2 at two different magnifications are given in Fig. 2 (a, b). The spherical, well-defined particles have an average diameter less than 10 nm. The addition of PEG is believed to account for the small particle size. However, slight particle agglomeration is also observed since PEG acts both as fuel and surfactant. Fig. 2(c) shows the HRTEM image of the $CoFe_2O_4$ nanoparticles. Here, the well-defined lattice fringes are observed and the measured d-spacings are 0.126, 0.214, and 0.303 nm, which coincide with the d spacing observed from XRD patterns. In addition, white spaces are noticed in the HRTEM images, indicating the presence of empty spaces with a diameter of approximately 3-4 nm. These spaces may enhance the accessibility of electrolyte ions into the electrode material. Similarly, the nanoparticulate size supports an increase in the active site of the active material, leading to a high capacitance. Fig. 2(d) shows the TEM image of rGO prepared using the hydrothermal method. The transparency of rGO reveals several layers of rGO sheets. In addition, the observed wrinkles confirm the good flexibility of rGO.

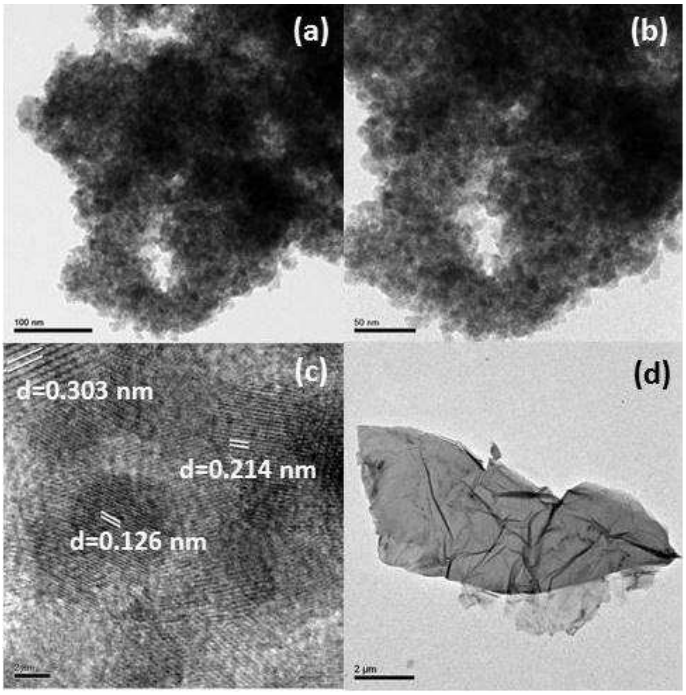

Fig. 2. (a, b) TEM images at different magnifications, (c) HRTEM image and (d) TEM image of $CoFe_2O_4$ nanoparticles.

Electrical Properties

Fig. 3 shows the Cole-Cole plot of the prepared $CoFe_2O_4$ particles at different PEG concentrations. It can be seen that a single semicircle, with a different diameter, is observed in all cases, indicating the conductivity is due to the grain interior. It is well known that the diameter of the semicircle is indicative of the bulk resistance of the material. In the present case, CC-2 has a smaller diameter than CC-1 and CC-3, suggesting it has a higher electrical conductivity. The calculated d.c. electrical conductivity is 9.1 x 10^{-6} S cm^{-1} for CC-1, 3.43 x 10^{-5} S cm^{-1} for CC-2 and 1.36 x 10^{-5} S cm^{-1} for CC-3. The obtained high conductivity of CC-2 may be due to the larger grain size, since it is well reported that a larger grain size reduces the grain boundary effect, which in turn yields higher conductivity.[21] The calculated capacitance from the Cole-Cole plot is 53,

30, and 18 pF for CC-1, CC-2, and CC-3, respectively. These values confirm the grain boundary effect on the conducting mechanism.[22] Based on the conductivity analysis, the CC-2 was considered the optimal electrode material for further electrochemical analysis.

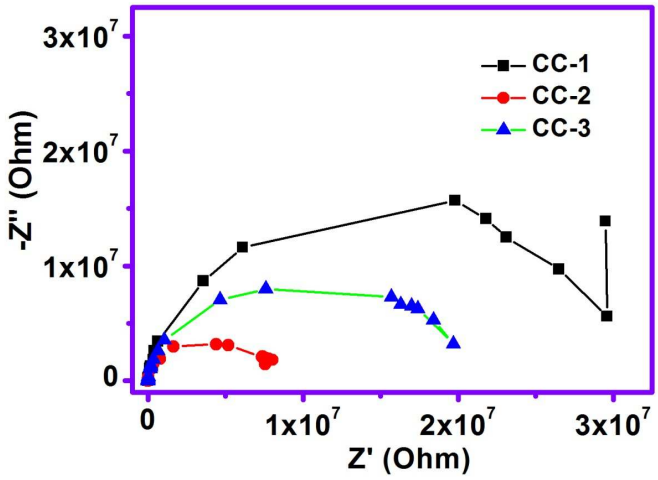

Fig. 3. Cole-cole plot of $CoFe_2O_4$ particles at room temperature.

Electrochemical Properties of $CoFe_2O_4$ electrode

The electrochemical performance of $CoFe_2O_4$ electrode was investigated using cyclic Voltammetry (CV), galvanostatic charge-discharge (GCD) and electrochemical impedance spectroscopy (EIS) analysis. Fig. 4(a) shows the CV curve of CC-2 in 1M KOH electrolyte at scan rates of 1, 2, 5, 10 and 20 mV s^{-1} in the potential range 0 to -1.1 V *vs* Hg/HgO. A potential dependent and a potential independent current region is observed. The potential independent region indicates charge storage phenomena based on the formation of an electrical double layer, supporting the capacitance contribution by redox reactions. The observed redox peaks at -1.04V/-0.63V *vs* Hg/HgO confirm the redox reaction between Fe^{3+} and Fe^{2+} ions,[23] revealing that charge is stored in $CoFe_2O_4$ electrodes predominantly by this redox reaction. The calculated specific capacitance is 195 Fg^{-1} at 1 mV s^{-1}. Further increasing the scan rate, the peak shift and peak broadening is observed due to the increase in electrode resistance, which is characteristic of pseudocapacitive materials.

The Power law and Trasatti plot are used to further identify the surface charge storage mechanism and the amount of charge stored on the surface of the $CoFe_2O_4$ electrode, respectively. It is well known that there are three different mechanisms involved in charge storage such as (i) Faradaic reaction through intercalation/de-intercalation of ions, (ii) Faradaic reaction through surface redox reaction, and (iii) electric double layer (EDLC) formation at the electrode/electrolyte interface. It is also well known that the capacitive mechanism consists of (i) pseudocapacitive via surface redox reaction and (ii) EDL formation. According to Power's law, the scan rate dependent CV current can be expressed as[24-26]

$$i = av^b \quad (1)$$

Where, ν is scan rate (V s^{-1}), *a* and *b* are the adjustable parameters. The value of *b* is calculated from the slope of log *i* *vs* log *v* (Fig. 4(b)) at a fixed potential (V). It has been reported that if the calculated *b*-value is 0.5, the obtained CV current obeys the intercalation/de-intercalation mechanism, while if the *b*-value is 1, the obtained CV current is due to a capacitive mechanism. But the capacitive current is the combination of pseudocapacitive and EDLC current. Fig. 4(c) shows the plot between the *b*-value at each measured potential. It can be seen that the calculated *b*-value is closer to 1. Hence, it may be concluded that the charge storage mechanism in $CoFe_2O_4$ is capacitive rather than intercalation/de-intercalation.

The capacitive and intercalation current with respect to potential can be measured using the following equation[24-26]

$$i(V) = s_1 v + s_2 v^{1/2} \quad (2)$$

This can be modified into

$$i(V)/v^{1/2} = s_1 v^{1/2} + s_2 \quad (3)$$

Where, $s_1\upsilon$ and $s_2\upsilon^{1/2}$ represent the current contribution from capacitive and intercalation of ions, respectively. The value of s_1 and s_2 are found from the slope and intercept of the plot between $i(V)/\upsilon^{1/2}$ and $\upsilon^{1/2}$. The representative curve of $i(V)/\upsilon^{1/2}$ *vs* $\upsilon^{1/2}$ at -0.65V is shown in Fig. 4(d). Fig. 4(e) further shows that the maximum amount of charge storage is due to the capacitive mechanism rather than an intercalation mechanism in $CoFe_2O_4$ electrodes. At a low scan rate, the electrode possesses only a minor amount of specific capacitance due to intercalation current, while this is negligible at a high scan rate. Hence, the $CoFe_2O_4$ electrode stores the charge based on the capacitive mechanism at high scan rate.

The amount of charge stored in the inner and outer surface of the electrode is calculated using Trasatti plot.[27] Commonly, the total amount (Q_{total}) of charge stored in the electrode is due to the sum of the charge storage contribution from the inner (Q_{in}) and outer (Q_{out}) surface of the electrode. Fig. 4 (f, g) shows the Trasatti plot of $CoFe_2O_4$ electrodes. The y-intercept of the linear fit of 1/q *vs* $\nu^{1/2}$ at ν=0 represents the total amount of charge stored in the electrode (Fig. 4(f)). At a low scan rate, the electrolyte ions having unlimited accessible time into the electrode, therefore a large amount of charge is stored on both inner and outer surfaces of the electrode. The y-intercept of the linear fit of q *vs* $\nu^{-1/2}$ at $\nu=\alpha$ shows the amount of charge stored at the outer surface of the electrode (Fig. 4(g)). At high scan rate, the electrolyte ions access only the outer surface of the electrode due to the limited interaction time with electrode. The charge storage contribution from inner electrode is calculated as $Q_{total}–Q_{out}$. According to the Trasatti plot (Fig. 4(f, g)), the amount of charge stored in the inner and outer surface of the electrode is 334 and 98 C g^{-1}, respectively. Overall, it can be concluded that the capacitive mechanism is the dominant process for storing charge in the electrode and the presence of porosity facilitates charge storage on the inner surface of the electrode.

Fig. 5(a) shows the galvanostatic charge-discharge (GCD) curves of $CoFe_2O_4$ at different current densities. Three different regions are observed: the potential dependent regions [I (-1 to -0.65V *vs* Hg/HgO) and III (-0.50 to -0V vs Hg/HgO)] and a potential independent region [II (-0.65 to -0.50V *vs* Hg/HgO)]. The potential dependent variation with time reveals that the charge storage is due to the double layer formation *i.e.* electrostatic adsorption of electrolyte ions at the electrode/electrolyte interface (region I and III). Similarly, the independent variable of time with potential (region II) describes that the charge storage of electrode is due to the redox reaction between Fe^{3+} and Fe^{2+} ions. As noted earlier, the charge storage is mainly due to the capacitive mechanism rather than the intercalation mechanism. The discharge time decreases with increasing current density leading to a decrease in specific capacitance of the electrode, since the time available for the electrolyte ions to access the electrode is lower at high current densities.[28-30]

Fig. 5(b) represents the variation of specific capacitance with current density. The $CoFe_2O_4$ delivers the specific capacitance of 125 F g^{-1} at 0.5 A g^{-1}. The decrease in specific capacitance with increasing current density can be explained by: (i) the long interaction time between $CoFe_2O_4$ electrode and electrolyte ions at low current density allows storage of a large amount of charge in the electrode, providing high specific capacitance; and (ii) at high current density, the interaction time of the electrolyte ions with electrode is limited. Hence, low specific capacitance is yielded at high current densities.

The charge storage kinetics at the electrode/electrolyte interface was analyzed using electrochemical impedance analysis (EIS) at near peak potential ((Fig. 5(c, d)). The electrode behaves as a resistor and capacitor at high and low frequency regions, respectively.[31,32] In general, the EIS spectra consists of three different regions (i) high frequency (intersection of semicircle represents the equivalent serial resistance (R_{ESR})), (ii) mid frequency (diameter of the semicircle shows the charge transfer resistance at the electrode/electrolyte interface (R_{ct})), and (iii) low frequency region (capacitive region, which also supports the observation of the charge storage mechanism of the electrode *via* the angle of tail from real axis).[32]

Fig. 5(e) shows that the R_{ct} value is decreased with increasing potential from -0.5V to -0.85 V. It confirms that the charge is transferred easily at the electrode/electrolyte interface, due to accessibility of the electrolyte ions within the electrode. However, the R_{ESR} value is small at the peak potential because of the fast transfer of electrons at this potential. On the other hand, Fig. 5(f) represents the variation of phase angle with applied potential. It is well known that as phase angle approaches 90˚, it is the typical electric double layer formation that leads to lower diffusive resistance. In contrast, for pseudocapacitive mechanism, the tail reaches a 45˚ angle, having a higher diffusive resistance. In the case of the tail having the phase angle between 90 to 45˚, the system stores the charge in both the mechanisms. In this present case, the EDL capacitive mechanism is dominant in the potential range between -0.5 and -0.6 V, and -0.7 and -0.85 V, since the phase angle is close to 90˚. On the other hand, at -0.65 V, the phase angle is 57˚, which reveals the presence of a pseudocapacitive mechanism ((Fig. 5(f)). This potential corresponds to the peak potential of $CoFe_2O_4$ which is in agreement with the CV results. Hence, it can be concluded that $CoFe_2O_4$ is a suitable negative electrode based on good electrical conductivity, good electrochemical performance, and material porosity.

Electrochemical performances of fabricated Asymmetric Supercapacitor(ASC)

The asymmetric supercapacitor is fabricated using $CoFe_2O_4$ as negative electrode, reduced graphene oxide (rGO) as positive electrode and 1M KOH as the aqueous electrolyte. The main advantages of the asymmetric supercapacitor are an enhanced working potential window, and high specific capacitance and energy density.[33,34] Figure 6 shows the CV curves of the individual electrodes of $CoFe_2O_4$ and rGO at 2 mV s^{-1}. It can be seen that the rGO exhibits rectangular curve that infers the ideal capacitive behaviour, which stores the charge based on surface adsorption of electrolyte ions via electrostatic interaction or non-Faradaic reaction on the electrode/electrolyte interface. The calculated specific capacitance of rGO is 274 Fg^{-1} at 2 mV s^{-1}. In addition, there is no obvious distortion of CV curve at the edge of switching potential which infers the low electrode resistance of rGO.

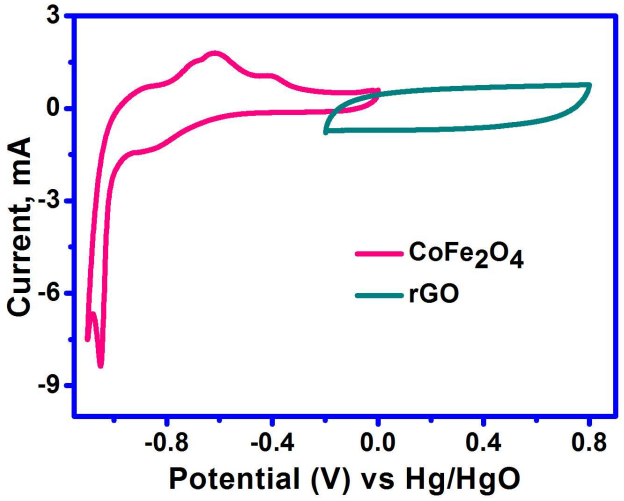

Fig. 6 Comparative CV curves of $CoFe_2O_4$ and rGO at 2 mV s^{-1}.

In order to counterbalance the specific capacitance and energy density of the device, the mass balance is calculated using eqn. 4 and the obtained mass ratio between $CoFe_2O_4$ and rGO is ca.0.77.

$$\frac{m_+}{m_-} = \frac{C_- \times \Delta V_-}{C_+ \times \Delta V_+} \qquad (4)$$

Fig. 7(a) shows the CV curves of the $CoFe_2O_4$||rGO asymmetric supercapacitor measured at different scan rates of 5, 10, 20, 30, 40 and 50 mV s^{-1} with potential range of 0 to 1.5 V. The CV curve shows the ideal capacitive behaviour, even at 50 mV s^{-1}, revealing good electrochemical reversibility of the device. The calculated gravimetric capacitance is 31.3 Fg^{-1} at 5 mV s^{-1}. Further, the GCDs curve does not show any IR or potential drop at the beginning of discharge curve, suggesting a negligible loss of energy of the device. In addition, the discharge time is decreased with increasing current densities ((Fig. 7(b)). The device exhibits the specific capacitance of 38 F g^{-1} at 3 mA cm^{-2}. In addition, the specific capacitance of the device is decreased with increasing current density due to the insufficient accessible time of electrolyte ions to the electrodes ((Fig. 7(c)). The energy and power densities of the asymmetric supercapacitor are calculated based on the total mass of the electrodes. The device exhibits the gravimetric energy density of 12.14 Wh kg^{-1} at a power density of 643 W kg^{-1} ((Fig. 7(d)). The energy density is higher than the reported ASCs of MnO–rGO||functionalized carbon (2.6 Wh kg^{-1}),[35] Polypyrrole||MnO_2,[36] $MnFe_2O_4$||$LiMn_2O_4$ (10 Wh kg^{-1}),[37] AC||MnO_2 (10 Wh kg^{-1}),[38] Fe_3O_4||MnO_2 (8.1 Wh kg^{-1}),[39] and V_2O_5 nanowire/CNT||MnO_2/C (16 Wh kg^{-1})[40].

Further, to understand the charge transfer kinetics at the electrode/electrolyte interface, EIS analysis was carried out both before and after cycling (Fig. 7(e)). The inset shows the Randle mathematical model circuit for fitting the experimental data. It can be seen that the model circuit fits experimental values well. Here, R_{ESR} represents the equivalent serial resistance, R_{ct} is the charge transfer resistance at the electrode/electrolyte interfaces during electrochemical reaction, C_{dl} and C_f corresponds to the double layer capacitance and Faradaic capacitance respectively, and W_d is the diffusive of Warburg resistance of electrolyte ions into the electrode. Before and after cycling, the fitted R_{ESR} and R_{ct} values are 0.612 and 1.249 ohm and 6.965 and 6.995 ohm, respectively. Even after 3000 cycling, there is no significant change of charge transfer resistance observed, suggesting that the fabricated device is suitable for energy storage applications.

Fig. 7f shows the cycle life of the fabricated ASC up to 3000 cycles at 7 mA cm^{-2}. The $CoFe_2O_4$||graphene device exhibits long-term cyclic stability with the capacitance loss of 33% over 3000 cycles. This is comparable, and in some cases an improvement on, reported values for similar devices. Capacitance retention of 71.9% over 2500 cycles for

carbon/$NiCo_2S_4$||AC is reported.[41] The $La_{0.7}Sr_{0.3}CoO_{3-\delta}$||AC device delivered 80% of specific capacitance retention after 2000 cycles.[42] Ruibin *et al* have reported that the monodisperse carbon microspheres||rGO delivered 75% of initial specific capacitance after 1000 cycles.[43] The $Ni(OH)_2$/ultrathin-graphite foam||activated microwave exfoliated graphite oxide showed 63.2% of specific capacitance retention over 10000 cycles.[44] CSS/Graphite/PEDOT/MnO_2||AC exhibited 81% of specific capacitance over 2000 cycles.[45] The capacitance loss in this study may be due to the decrease of electrolyte ions and loss of electrical contact between active material and the substrate. The inset figure shows typical charge-discharge curves at initial and final cycle. The charge-discharge curves maintain the symmetric and linear charge-discharge behaviour, revealing good electrochemical reversibility of the device. Further, the four fabricated devices are serially connected, illuminating the LED for long duration (10 mins) (Fig. 8), which is comparable to the reported time.[46-48]

Overall, the good performance of $CoFe_2O_4$||graphene device is observed. This may be attributed to i) porous morphology, which facilitates greater contact of electrolyte ions during charging/discharging process, ii) good electrical conductivity, and iii) best combination of positive and negative electrodes. The suitability of the device for supercapacitor applications is demonstrated.

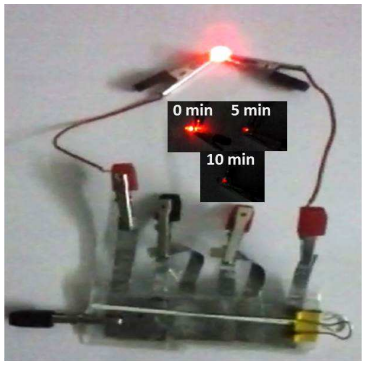

Fig. 8. Glowing LED using serially connected three asymmetric supercapacitor. (inset) Glowing LED at different time intervals.

4. Conclusion

The effective role of PEG in the synthesis of $CoFe_2O_4$ nanoparticles is identified. The formation of single phase $CoFe_2O_4$ particles is evidenced by XRD and FT-IR analysis. The porous morphology is observed from FE-SEM images. The sample possesses good electrical conductivity of 3.43 x 10^{-5} S cm^{-1} at room temperature. The pseudocapacitive nature of the $CoFe_2O_4$ is explained using Power's law and Trasatti plot. The $CoFe_2O_4$ exhibits maximum specific capacitance of 195 Fg^{-1} at 1 mVs^{-1}. Similarly, the amount of charge stored in the inner (334 Cg^{-1}) and outer surface (98 Cg^{-1}) of the electrode is calculated. The combination of $CoFe_2O_4$ and rGO as suitable electrodes for hybrid capacitors was demonstrated and tested for real time application through a glowing LED for 10 minutes.

Acknowledgement

The authors would like to thank Department of Science and Technology (DST-SERB), Government of India, for providing financial support (SR/FTP/PS-80/2009) under the ''Fast Track Young Scientist'' scheme.

Notes and References

[a] *Solid State Ionics and Energy Devices Laboratory, Department of Physics, Bharathiar University, Coimbatore – 641 046, Tamil Nadu, India.*
[b] *School of Chemical and Mathematical Sciences, Murdoch University, Murdoch, WA 6150, Australia*
*(*E-mail: selvankram@buc.edu.in)*

References

[1] B.E. Conway, Electrochemical Supercapacitors, Scientific Fundamentals and Technology Applications, Kluwer Academic/Plenum Press, New York, 1999.
[2] F. Béguin, E. Frqckowiak, Supercapacitors Materials, Systems, and Applications. Wiley-VCH Verlag GmbH & Co. KGaA, Boschstr. 12, 69469 Weinheim, Germany, 2013.
[3] K.V. Sankar, R.K. Selvan, RSC Adv. 2014, 4, 17555-17566.
[4] B. Senthilkumar, K.V. Sankar, C. Sanjeeviraja, R.K. Selvan, J. Alloys Comp. 2013, 553, 350-357.
[5] A. Shanmugavani, R.K. Selvan, RSC Adv. 2014, 4, 27022-27029.
[6] K. V. Sankar, R.K. Selvan, J. Power Sources 2015, 275, 399-407.
[7] P. Xiong, H. Huang, X. Wang, J. Power Sources 2014, 245, 937-946.
[8] W. Wang, Q. Hao, W. Lei, X. Xia, X. Wang, J. Power Sources 2014, 269, 250-259.
[9] L. Wu, Q. Xiao, Z. Li, G. Lei, P. Zhang, L. Wang, Solid State Ionics 2012, 215, 24–28.
[10] Y. Wang, D. Su, A. Ung, J. Ahn, G. Wang, Nanotechnology 2012, 23, 055402-055408.
[11] Y. Xu, W. Bian, J. Wu, J. Tian, R. Yang, Electrochim. Acta 2015, 151, 276–283.

[12] S. Jovanović, M. Spreitzer, M. Otoničar, J. H. Jeon, D. Suvorov, J. Alloys Comp. 2014, 589, 271-277.
[13] V. Georgiadou, C. Kokotidou, B. L. Droumaguet, B. Carbonnier, T. C. Papadopoulou, C. D. Samara, Dalton Trans. 2014, 43, 6377–6388.
[14] S. Yoon, J. Appl. Electrochem. 2014, 44, 1069–1074.
[15] (a). K. Vasundhara, S. N. Achary, S. K Deshpande, P. D. Babu, S. S. Meena, A. K. Tyagi, J. Appl. Phys. 2013, 113, 194101-194109. (b). M. R. Barati, S. A. S. Ebrahimi, A. Badiei, J. Non-Cryst. Solids 2008, 354, 5184-5185. (c). H. Birol, C. R. Rambo, M. Guiotoku, D. Hotza, RSC Adv. 2013, 3, 2873-2884.
[16] W. Pon-On, N. Charoenphandhu, I. Tang, P. Jongwattanapisan, N. Krishnamra, R. Hoonsawat, Mater. Chem. Phys. 2011, 131, 485-494.
[17] C. Borgohain, K.K. Senapati, K.C. Sarma, P. Phukan, J. Mol. Catal. A: Chem. 2012, 363-364, 495-500.
[18] S. Li, B. Wang, J. Liu, M. Yu, Electrochim. Acta 2014, 129, 33-39.
[19] E.R. Kumar, R. Jayaprakash, T. Prakash, J. Magn. Magn. Mater. 2014, 358-359, 123-127.
[20] (a). Y. Liu, Y. Zhang, J.D. Feng, C.F. Li, J. Shi, R. Xiong, J. Exp. Nanosci. 2009, 4, 159-168. (b). S. Ayyappan, S. Mahadevan, P. Chandramohan, M. P. Srinivasan, J. Philip, B. Raj, J. Phys. Chem. C 2010, 114, 6334–6341. (c). V. Georgiadou, V. Tangoulis, I. Arvanitidis, O. Kalogirou, C. D. Samara, J. Phys. Chem. C 2015, 119, 8336-8348.
[21] S.Brahma, R.N.P.Choudhary, A.K. Thakur, Physica B 2005, 355, 188-201.
[22] R. Amin, C. Lin, J. Peng, K. Weichert, T. Acarturk, U. Starke, J. Maier, Adv. Funct. Mater. 2009, 19, 1697-1704.
[23] D. Guan, Z. Gao, W. Yang, J. Wang, Y. Yuan, B. Wang, M. Zhang, L. Liu, Mater. Sci. Eng. B 2013, 178, 736-743.
[24] M. Sathiya, A.S. Prakash, K. Ramesh, J.M. Tarascon, A.K. Shukla, J. Amer. Chem. Soc. 2011, 133, 16291-16299.
[25] J. Duay, S.A. Sherrill, Z. Gui, E. Gillette, S.B. Lee, ACS Nano 2013, 7, 1200-1214.
[26] H. Yina, C. Song, Y. Wang, S. Li, M. Zeng, Z. Zhang, Z. Zhu, K. Yu, Electrochim. Acta 2013, 111, 762-770.
[27] B. Senthilkumar, K. V. Sankar, C. Sanjeeviraja, R. K. Selvan, J. Alloys Comp. 2013, 553, 350–357.
[28] K. V. Sankar, D. Kalpana, R. K. Selvan, J. Appl. Electrochem. 2012, 42, 463-470.
[29] K. V. Sankar, S. T. Senthilkumar, L. J. Berchmans, C. Sanjeeviraja, R. K. Selvan, Appl. Surf. Sci. 2012, 259, 624–630.
[30] S. Vijayakumar, S. Nagamuthu, G. Muralidharan, ACS Appl. Mater. Inter. 2013, 5, 2188–2196.
[31] X. Zhang, Z. Lin, B. Chen, S. Sharma, C. P. Wong, Z. Zhang, Y. Deng, J. Mater. Chem. A 2013, 1, 5835–5839.
[32] Y. He, W. Chen, X. Li, Z. Zhang, J. Fu, C. Zhao, E. Xie, ACS Nano 7 (2013) 174–182.
[33] Z.S. Wu, W. Ren, D.W. Wang, F. Li, B. Liu, H.M. Cheng, ACS Nano 2010, 4, 5835-5842.
[34] J. Ji, L.L. Zhang, H. Ji, Y. Li, X. Zhao, X. Bai, X. Fan, F. Zhang, R.S. Ruoff, ACS Nano 2013, 7, 6237-6243.
[35] D. Antiohos, K. Pingmuang, M. S. Romano, S. Beirne, T. Romeo, P. Aitchison, A. Minett, G. Wallace, S. Phanichphant, J. Chen, Electrochim. Acta 2013, 101, 99–108.
[36] V. Khomenko, E. Raymundo-Pinero, E. Frackowiak, F. Beguin, Appl. Phys. A 2006, 82, 567–573.
[37] Y. P. Lin, N. L. Wu, J. Power Sources 2011, 196, 851–854.
[38] T. Brousse, P. L. Tabern, O. Crosnier, R. Dugas, P. Guillemet, P. Scudeller, Y. Zhoud, F. Favier, D. Belanger, P. Simon, J. Power Sources 2007, 173, 633–641.
[39] T. Cottineau, M. Toupin, T. Delahaye, T. Brousse, D. Belanger, Appl. Phys. A 2006, 82, 599–606.
[40] B.Z. Chen, Y. Qin, D. Weng, Q. Xiao, Y. Peng, X. Wang, H. Li, F. Wei, Y. Lu, Adv. Funct. Mater. 2009, 19, 3420–3426.
[41] H. Wang, C. Wang, C. Qing, D. Sun, B. Wang, G. Qu, M. Sun, Y. Tang, Electrochim. Acta 2015, 174, 1104–1112.
[42] Y. Cao, B. Lin, Y. Sun, H. Yang, X. Zhang, Electrochim. Acta 2015, 178, 398–406.
[43] Q. Ruibin, H. Zhongai, Y. Yuying, L. Zhimin, A. Ning, R. Xiaoying, H. Haixiong, W. Hongying, Electrochim. Acta 2015, 167, 303–310.
[44] J. Ji, L. L. Zhang, H. Ji, Y. Li, X. Zhao, X. Bai, X. Fan, F. Zhang, R. S. Ruoff, ACS Nano 2013, 7, 6237-6243.
[45] P. Tang, L. Han, L. Zhang, ACS Appl. Mater. Interfaces 2014, 6, 10506−10515.
[46] L.F. Chen, Z.H. Huang, H.W. Liang, Q.F. Guan, S.H. Yu, Adv. Mater. 2013, 25, 4746–4752.
[47] C. Dong, Y. Wang, J. Xu, G. Cheng, W. Yang, T. Kou, Z. Zhang, Y. Ding, J. Mater. Chem. A 2014, 2, 18229-18235.
[48] T. Zhai, F. Wang, M. Yu, S. Xie, C. Liang, C. Li, F. Xiao, R. Tang, Q. Wu, X. Lu, Y. Tong, Nanoscale 2013, 5, 6790-6796.

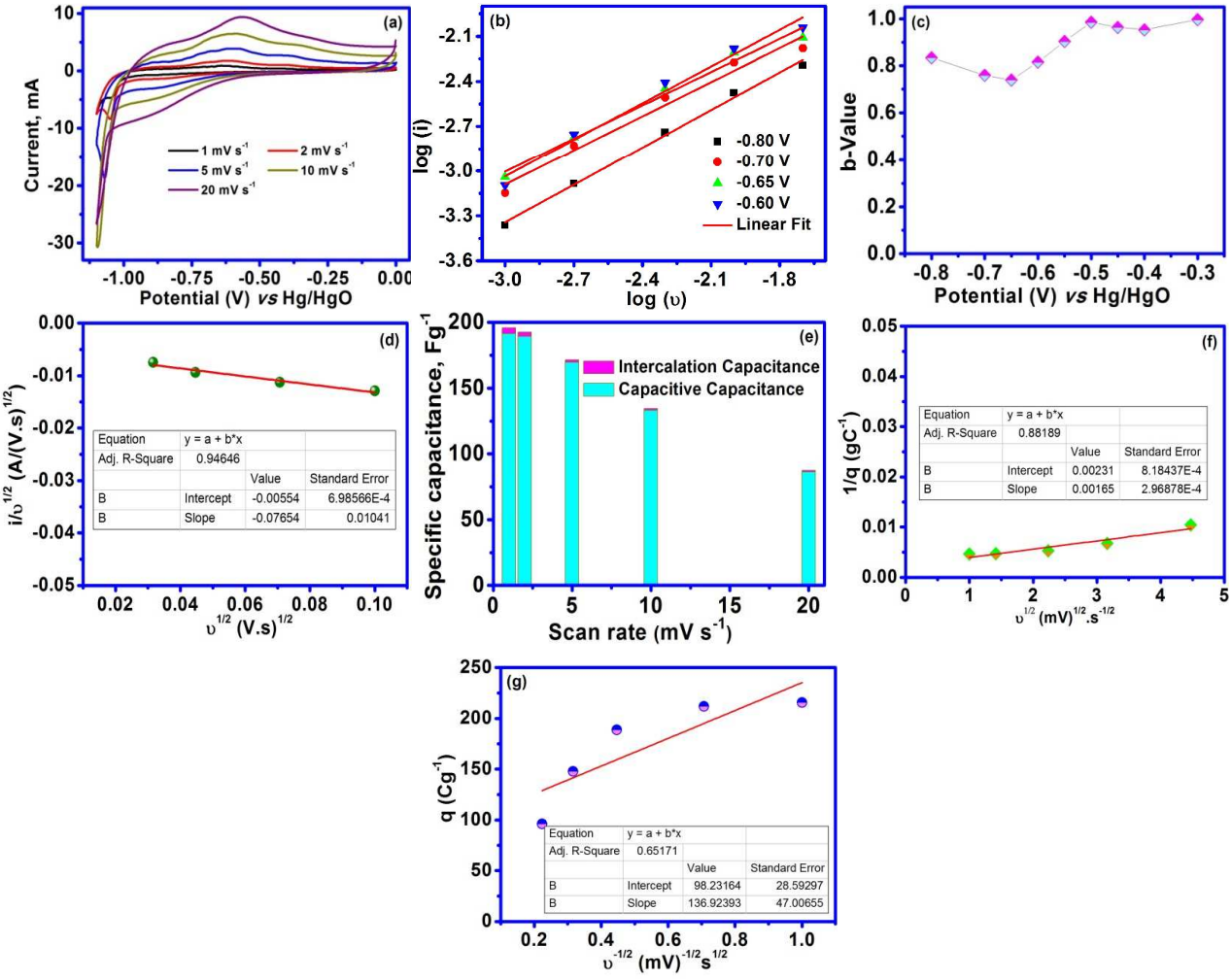

Fig. 4. (a) CV curves of $CoFe_2O_4$ at different scan rates, (b) plot between log (i) vs log (scan rate), (c) variation of b-values with applied potential, (d) the plot between $i/v^{1/2}$ and $v^{1/2}$ at -0.65 V, (e) variation of specific capacitance (intercalation and de-intercalation specific capacitance) as a function of scan rate, and (f, g) Corresponds to the Trasatti plot.

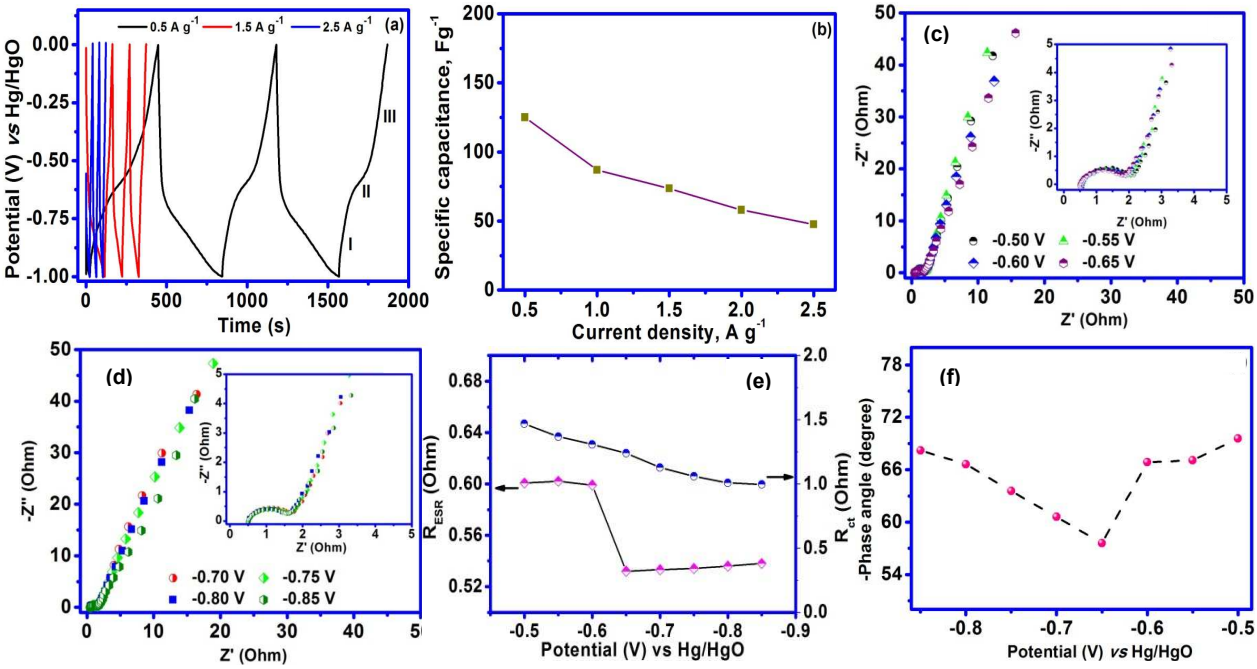

Fig. 5. (a) GCDs curves of porous $CoFe_2O_4$ at different current densities, (b) Variation of specific capacitance with current densities, (c, d) Nyquist plot of $CoFe_2O_4$ at different potentials, (e) Variation R_{ESR} and R_{ct} as a function of applied potential, and (f) Variation of phase angle with respect to applied potential.

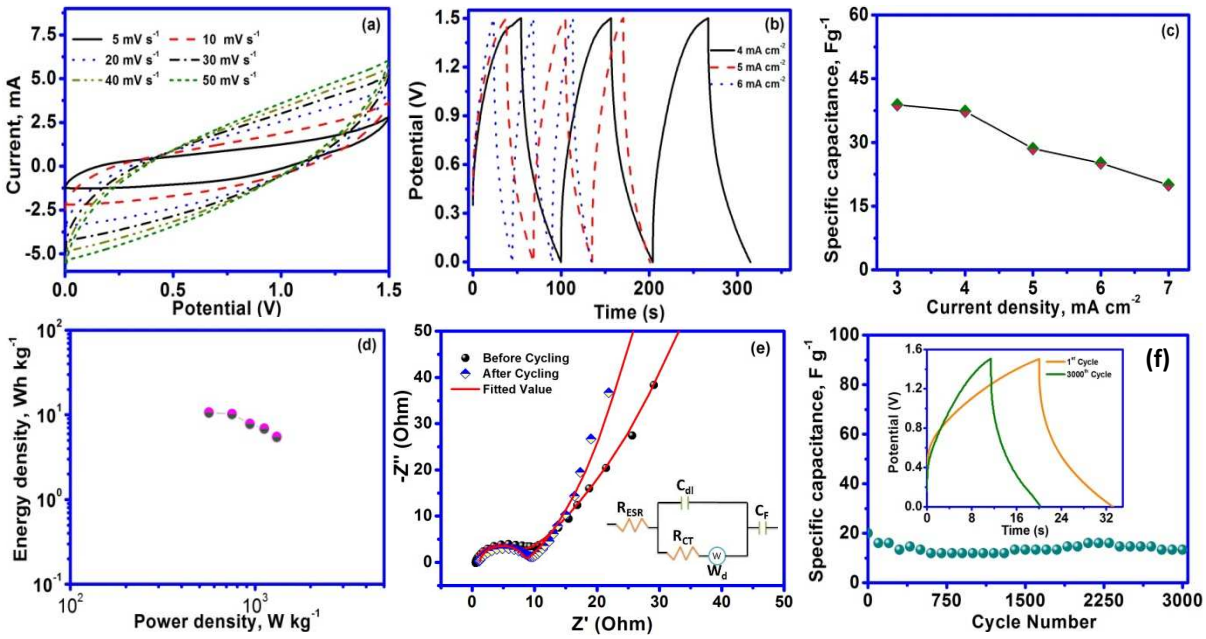

Fig. 7. (a, b) CV and GCDs curves of fabricated asymmetric supercapacitor at different scan rates and current densities, (c) variation of specific capacitance with current densities, (d) Ragone plot of (plot between energy density and power density) the fabricated device, (e) Nyquist spectra of asymmetric cell (Inset: Randles model circuit) and (f) Cyclic stability of the fabricated asymmetric supercapacitor over 3000 cycles. The inset is corresponding initial and final cycle of the device.

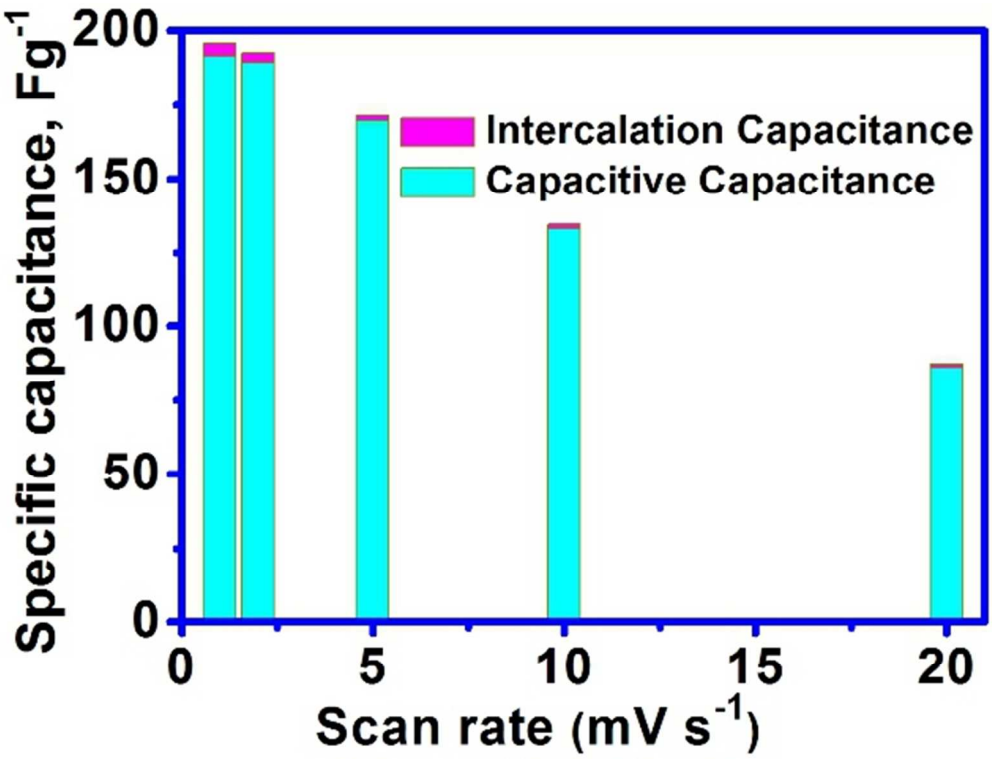

107x81mm (150 x 150 DPI)